

Synthesis and physical properties of Na_xTO_2 ($\text{T}=\text{Mn}, \text{Co}$) nanostructures for cathode materials in Na-ion batteries

Mahesh Chandra,^{1,*} Rishabh Shukla,^{1,*} Muhammad Rashid,¹ Amit Gupta,² Suddhasatwa Basu,³ and R. S. Dhaka^{1,†}

¹*Department of Physics, Indian Institute of Technology Delhi, Hauz Khas, New Delhi-110016, India*

²*Department of Mechanical Engineering, Indian Institute of Technology Delhi, Hauz Khas, New Delhi-110016, India*

³*Department of Chemical Engineering, Indian Institute of Technology Delhi, Hauz Khas, New Delhi-110016, India*

(Dated: December 31, 2021)

We prepared Na_xTO_2 ($\text{T} = \text{Mn}, \text{Co}$) nanostructures to use as cathode material in Na-ion batteries. The Rietveld refinement of x-ray diffraction data confirms the hexagonal symmetry. Scanning and transmission electron microscopy measurements show hexagonal and rod-shape morphology for $\text{T} = \text{Co}$ and Mn , respectively. The magnetic measurements indicate the presence of variable oxidation states of Mn/Co ions, but no long range ordering till 5 K. We find that the $\text{Na}_{0.6}\text{MnO}_2$ is highly insulating whereas $\text{Na}_{0.7}\text{CoO}_2$ is semiconducting in nature. The conduction in $\text{Na}_{0.7}\text{CoO}_2$ takes place through both variable range hopping (VRH) as well as activation mechanisms in different temperature ranges. However, for $\text{Na}_{0.6}\text{MnO}_2$ the VRH prevails at elevated temperatures. Furthermore, the coin cells have been fabricated and tested the electrochemical behavior using cyclic voltammetry, which confirms the reversibility of Na-ions during intercalation/de-intercalation.

Keywords: Na-ion battery materials; transition-metal oxides; physical properties

INTRODUCTION

In recent years, rechargeable batteries are of high demand for powering portable electronic devices as well as electric vehicles. Therefore, searching for high performance electrode materials for Na-ion batteries has attracted great attention due to its abundance in nature and low cost raw materials for large scale energy storage applications [1, 2]. Among the materials used for electrodes (cathode/anode) in electrochemical energy storage devices, transition metal (TM) oxides are most suitable compounds owing to their layered structure and variable oxidation state of TM ions [1, 3, 4]. The layered structure allow a smooth insertion and deinsertion of Li^+/Na^+ during charging and discharging, whereas the valence of TM ion changes with addition or removal of the electrons through the external circuit. The structural stability of an electrode material is a crucial parameter as structural transformation in various layered materials has been observed during the battery cycling [5, 6]. In this direction, the LiCoO_2 in pristine as well as doped form [7, 8], is a well studied cathode material and extensively used in the Li-ion batteries [9, 10] and similarly the Na_xCoO_2 in Na-ion batteries [11]. However, considering the abundance of Mn and Fe in the Earth's crust, compounds based on these elements are particularly relevant for low cost energy storage in Na-ion batteries. On the other hand, the low cost LiMnO_2 is not thermodynamically stable in layered structure, but its Na counterpart, Na_xMnO_2 is stable in two structures, namely, O3 and P2 type structures [11]. In these structures, the lattice is built up by sheets of edge-sharing TO_6 octahedra and the alkali ions are inserted between these sheets with trigonal prismatic (P) or octahedral (O) environment [11]. The packing also differs in the number of sheets within the unit cell: 2 or

3, and the P2 and O3 phases have monoclinic distortions in their parent phases [12]. Due to a different migration pathway of Na-ion, P2-type structure gives better rate performance among these two structures [3]. A small change in the Na concentration which coupled with structure causes a significant change in the Na-ion dynamics, hence the electrochemical performance of the material in the battery. For example $\text{Na}_{0.67}\text{MnO}_2$ possesses a 2D layered structure whereas $\text{Na}_{0.44}\text{MnO}_2$ has a 3D tunnel type structure [13]. Also, a small change in Na content from 0.6 to 0.7 causes a metal to insulator transition in Na_xCoO_2 [14], which determines the electronic transport mechanism in these materials with temperature.

Apart from the Na stoichiometry the morphology also plays a key role in determining the capacity of the cathode materials [15–17]. Nanostructured materials have been found to improve the capacity of a Na-ion battery due to their large surface to volume ratio, which has a significant impact on diffusion of Na-ions in the solid phase. The material processing by various methods such as carbon coating, fluorination or microwave irradiation can also improve the electrochemical performance [18, 19]. The electrochemical potential of a cell, which determines the energy density of a battery is directly correlated with the valence state and electronic configuration of the electrode material. Therefore, in order to enhance the performance of an electrode material, an understanding of its physical ground states is vital. Despite being synthesized in 1971 by Parant *et al.* [20], the Na_xMnO_2 family has only recently been studied for its electrochemical properties owing to its potential as energy storage material. However, its physical properties such as electronic and magnetic ground states have largely been unexplored, which play a crucial role in determining the performance of Na-ion batteries. On

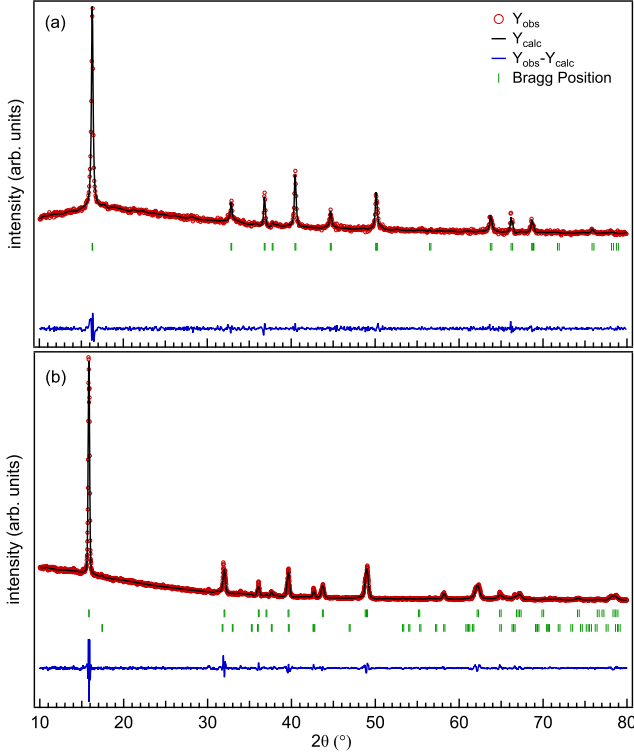


FIG. 1. Room temperature XRD pattern (red) and Rietveld refinement (black) of as-prepared (a) Na_xCoO_2 and (b) Na_xMnO_2 along with Bragg peaks and residual. The refinement is performed with hexagonal $\text{P6}_3/\text{mmc}$ space group (no. 194) and for Na_xMnO_2 an additional monoclinic phase has been used for better fitting.

the other hand, Na_xCoO_2 is well studied for its electrochemical properties as well as other physical properties such as thermoelectric, magnetic and electronic ground states, but obtaining a stable phase has always been a challenge due to its structural sensitivity towards moisture and air. The most stable structure of Na_xCoO_2 has been reported in the P2-phase ($0.67 \leq x \leq 0.72$).^[12] Here, we report the synthesis of the stable P2 phase of Na_xTO_2 ($\text{T} = \text{Mn}, \text{Co}$) nanostructures using sol-gel route and report their structural, morphological, electric transport and magnetic properties for Na-ion battery applications. In order to analyze the electrochemical behavior, cyclic voltammetry (CV) measurements were performed on fabricated coin cells and confirm the reversibility of Na^+ during intercalation/de-intercalation.

EXPERIMENTAL

We have synthesized Na_xTO_2 ($\text{T} = \text{Mn}, \text{Co}$) using a sol-gel method. Sodium acetate (99%), manganese acetate (99%), and cobalt acetate (99.9%) from Merck were added in a stoichiometric ratio in deionized water and homogeneously mixed via stirring for 2 hrs. Then the cal-

TABLE I. Rietveld refined (with $\text{P6}_3/\text{mmc}$ space group) parameters from the XRD data; H is hexagonal, M is monoclinic.

Sample	χ^2	$R_{wp}(\%)$	a (Å)	b (Å)	c (Å)	phase
$\text{Na}_{0.7}\text{CoO}_2$	1.15	18.3	2.824	2.824	10.928	H (100%)
$\text{Na}_{0.6}\text{MnO}_2$	2.35	22.8	2.875	2.875	11.193	H (80%)
			5.763	2.812	5.403	M (20%)

culated amount (molar ratio of 3:1) of citric acid (Sigma, 99.9%), used as a complexing agent was added to the solution with overnight stirring at 90°C , which results in the formation of gel. This gel was dried at 100°C for 12 hrs to low layered powder, and obtained powder then ground to fine particles. We finally sintered the powder at 700°C for 10 hrs to synthesize Na_xCoO_2 , whereas for Na_xMnO_2 the powder was preheated to 900°C for 12 hrs and then finally heating was done at 1100°C for 10 hrs. We performed the room temperature powder x-ray diffraction (XRD) with $\text{CuK}\alpha$ radiation (1.5406 \AA) from Panalytical X-ray diffractometer in the 2θ range of $10\text{--}85^\circ$. We analyzed the recorded XRD data by Rietveld refinement using Fullproof package, where the background was fitted using linear interpolation between data points. The surface morphology of the prepared materials has been investigated using a low magnification field effect scanning electron microscope (FE-SEM) at 20 keV electron energy. The transmission electron microscopy (TEM) measurements have been done with JEOL JEM-1400 Plus microscope at 120 keV. Raman spectra of prepared pellets were recorded with Renishaw inviaconfocal Raman microscope at wavelength of 532 nm and grating of 2400 lines/mm with 1 mW laser power on the sample. Transport properties and temperature and field dependent magnetic measurements were done using physical property measurement system (PPMS), and SQUID from Quantum Design, USA. For the electrochemical measurements, we have assembled the coin-cells of CR2016-type, with NaTO_2 ($\text{T} = \text{Mn}, \text{Co}$) as cathode, Na thin disk as anode, glass filter as a separator, and 1.0 mole NaClO_4 dissolved in ethylene carbonate (EC) and propylene carbonate (PC) (in 1:1 by volume) as the electrolyte. The cell assembly is carried out in the glove-box with water and oxygen content lower than 0.5 ppm, to avoid the oxidation and reaction with moisture. A battery cycler from Bio-Logic-VMP3 has been used for the cyclic voltammetry of the fabricated cells.

RESULTS AND DISCUSSION

The room temperature XRD patterns of as-synthesized Na_xTO_2 (Mn, Co) samples are shown in Fig 1. For the prepared Na_xCoO_2 sample [Fig. 1 (a)], all the peaks are well described by hexagonal $\text{P6}_3/\text{mmc}$ space group and the Rietveld refined lattice parameters are in good

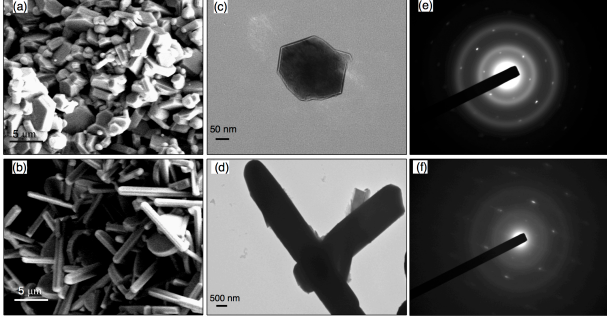


FIG. 2. (a-b) FE-SEM images, (c-d) TEM images, and (e-f) SAED patterns of as prepared Na_{0.7}CoO₂ and Na_{0.6}MnO₂ samples, respectively.

agreement with the values reported for the composition Na_{0.71}CoO₂ (JCPDS file No. 30-1182), which is the most stable P2-phase in the all possible structures of Na_xCoO₂ [12, 21]. The XRD pattern of Na_xMnO₂ [Fig. 1 (b)] is in agreement with that of P2-type Na_{0.6}MnO₂ [22] and the Rietveld refinement confirm the hexagonal structure with P6₃/mmc space group (194). However, there are few additional peaks observed in XRD pattern which corresponds to the α-NaMnO₂ (monoclinic) phase. We have included this phase in the refinement and find about 20% contribution, which is expected as the final sintering was done at high temperature in order to stabilize the P2-phase [20]. The lattice parameter extracted from the refinement are very well in agreement with the previously reported P2-Na_{0.6}MnO₂ [22]. We found that these samples have a stable structure when exposed to air and moisture at least up to the observed 60 days. The extracted lattice parameters for both the samples are summarized in table I. The ratio of Na and Mn/Co has been investigated (not shown) by energy dispersive x-ray spectroscopy (EDXS), which confirm the ratio of Na:Mn as 0.57:1 in Na_xMnO₂ sample. Our structural and EDXS analysis confirm that the Na_xMnO₂ sample is stabilized in P2-Na_{0.6}MnO₂ composition.

Figs. 2 (a-f) show the surface morphology of Na_xTO₂ (T = Mn, Co) samples, investigated using low magnification FE-SEM and TEM imaging techniques. The FE-SEM images [Figs. 2(a, b)] show the hexagonal and rod-shaped morphology for Na_{0.7}CoO₂ and Na_{0.6}MnO₂ samples, respectively. These structures are further investigated with the TEM [Figs. 2(c, d)], where we observed that the particle morphology in TEM is similar as in the FE-SEM, i. e., more accurately the Na_{0.7}CoO₂ in hexagonal particles of size about 200 nm, and the Na_{0.6}MnO₂ in rods of different thickness with a μm length. The selected area electron diffraction (SAED) pattern taken from these samples are shown in Figs. 2 (e, f). A hexagonal symmetry is observed in the recorded SAED patterns and the lattice constants deduced from the diffraction points (most intense) are comparable to the lattice

parameter from the Rietveld refinement and (002) peak of XRD patterns. However, the SEAD for Na_{0.7}CoO₂ which is synthesized at relatively low temperature than Na_{0.6}MnO₂ shows diffused rings as well as clear bright spots. We can not conclude from this that it is nanocrystalline but such pattern can possibly be originating from agglomerated crystals of various sizes [23]. In Fig. 3(a), we present the Raman spectrum of the Na_{0.6}MnO₂ sample, which shows the most prominent Raman mode at 650 cm⁻¹ along with other modes at 580, 460, and 350 cm⁻¹, as shown by the de-convoluted components by dashed lines. The mode at 580 cm⁻¹ corresponds to vibration of Mn-O-Mn in the stretching mode and indicates the presence of Mn⁴⁺ in the sample [24] whereas the peak at 650 cm⁻¹ is the characteristic of symmetric stretching vibrations of Mn-O bond [24–26]. Fig. 3(b) shows the room temperature Raman spectra for Na_{0.7}CoO₂, where we found that the Raman active modes can be identified as A_{1g} at 662 cm⁻¹ and E_{2g} at 462, 505, and 600 cm⁻¹. Iliev et. al. and others reported that the A_{1g} mode involve out of plane motions of only oxygen atoms in the CoO₆ octahedra, and E_{2g} modes are connected with both Na and O motions, whereas Co motions are not Raman active [27–29].

In order to get insight of the electronic transport properties, we have performed temperature dependent resistivity measurement from 380 K to 5 K (as shown in Fig. 4), which show the insulating nature for both these samples throughout the respective measured temperature range. Furthermore, we performed detailed analysis to extract the physical parameters, and fitted the temperature dependent resistance with two different conduction models namely, Arrhenius model:

$$\rho = \rho_0 \exp(E_a/k_B T)$$

where, E_a is the activation energy and other one is variable range hopping (VRH) model [30],

$$\rho = \rho_0 \exp(T_0/T)^{1/4}$$

where, T₀ is the characteristic temperature.

Here the Arrhenius model describes conduction by simple activation of charge carriers through the band gap between conduction and valance band, whereas VRH model prevails in disordered systems where potential fluctuation at spatially separated sites (due to disorder) assist the hopping of charge carriers. In VRH model, the characteristic temperature T₀ is related to the localization length and density of states near the Fermi level N(E) by the relation:

$$k_B T_0 = \left(\frac{18}{L^3 \times N(E)} \right)$$

where, L is the localization length.

First we discuss the electronic transport in Na_{0.7}CoO₂ and present the analysis in the inset of Fig. 4 (a), where

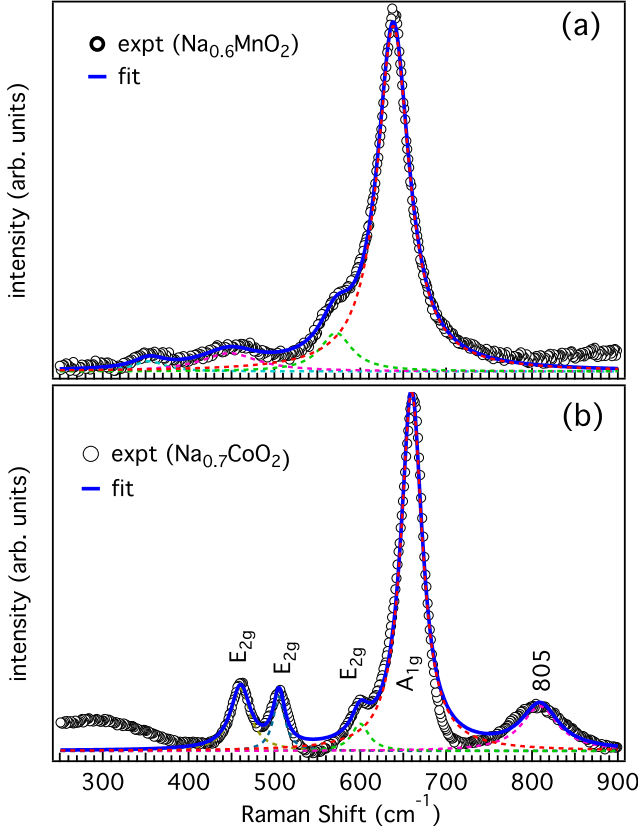


FIG. 3. Raman spectrum of (a) $\text{Na}_{0.6}\text{MnO}_2$, and (b) $\text{Na}_{0.7}\text{CoO}_2$ pellet, measured with $\lambda = 532$ nm at room temperature, along with the fitting using Lorentzian line shape.

TABLE II. Calculated values of characteristic temperature and density of states $N(E)$ by VRH model and activation energy E_a by Arrhenius model for Na_xTO_2 ($T = \text{Mn, Co}$).

Sample	VRH model		Arrhenius model
	$T_0(\text{K})$, $N(E)(\text{eV}^{-1}\text{cm}^{-3})$		E_a (meV)
$\text{Na}_{0.7}\text{CoO}_2$	3.02×10^5 , 9.1×10^{23}		64.8 ± 0.6
$\text{Na}_{0.6}\text{MnO}_2$	2.7×10^9 , 9.9×10^{18}		374 ± 5

the resistivity data are fitted well with the Arrhenius model at higher temperature range 365–300 K and with the VRH model at lower temperature range of 245–165 K [see Figs. 4(a2) and (a1), respectively]. We tried to fit the low temperature data with other models (such as adiabatic nearest neighbor hopping model of small polaron conduction and Schklovskii-Efros type of VRH with soft gap), but low temperature data of $\text{Na}_{0.7}\text{CoO}_2$ could not be fitted well with any of these models. Interestingly, the $\text{Na}_{0.6}\text{MnO}_2$ sample shows a highly insulating behavior as depicted from its high negative value of temperature coefficient of resistivity and a high resistivity at room temperature [Fig. 4 (b)]. Therefore, we could not measure

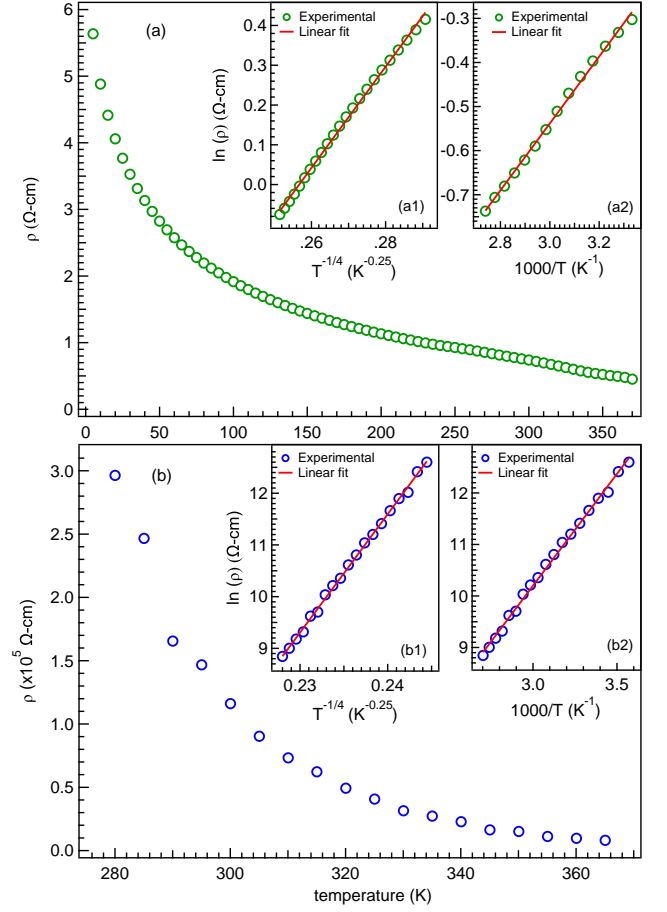


FIG. 4. Temperature dependent resistivity of (a) $\text{Na}_{0.7}\text{CoO}_2$ and (b) $\text{Na}_{0.6}\text{MnO}_2$ samples. The inset figures show the data fitted with VRH (a1, b1) and Arrhenius (a2, b2) models.

the resistivity of $\text{Na}_{0.6}\text{MnO}_2$ sample below 280 K as the value of resistivity went past the measurement limit of the instrument. The fitting to Arrhenius model in the temperature range between 380 K to 300 K gives the activation energy 374 ± 5 meV. However, such small band gap is expected to result in a semiconducting nature as in the case of α - NaMnO_2 ($E_a = 450$ meV) [13]. On the other hand, the data also fits well with the VRH model in the same temperature range, as shown in the inset of Fig. 4(b) for both the models in (b2) and (b1), respectively. The extracted parameters are summarized in the table II for both the samples and discussed below.

From the fitted data, the T_0 is quite large for $\text{Na}_{0.6}\text{MnO}_2$ compare to $\text{Na}_{0.7}\text{CoO}_2$ indicating a small localization length and/or smaller density of states. If we take the localization length comparable to the Mn/Co-O bond length we can get an estimate of density of states $[N(E)]$ near the Fermi level. By taking Mn-O and Co-O bond lengths 1.98 Å and 1.96 Å, respectively, for $\text{Na}_{0.6}\text{MnO}_2$ and $\text{Na}_{0.7}\text{CoO}_2$, we have calculated $N(E)$, as mentioned in the table II. Moreover, we found the most

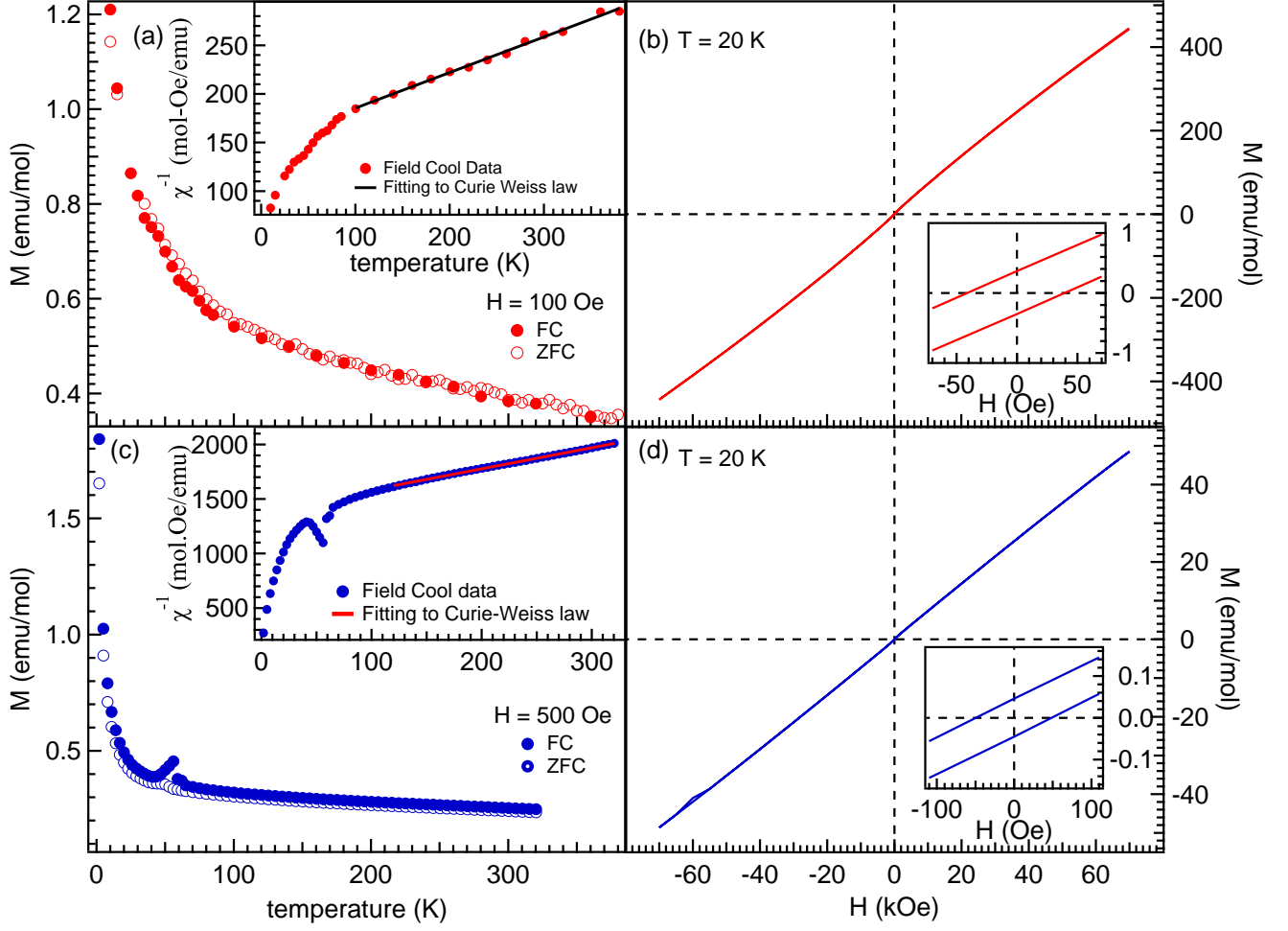


FIG. 5. The temperature dependent and isothermal magnetization of $\text{Na}_{0.6}\text{MnO}_2$ (a, b) and $\text{Na}_{0.7}\text{CoO}_2$ (c, d) samples. The insets in (a, c) show the Curie-Weiss fitting till 100-120 K. Insets in (b, d) show the zoomed view in the lower field range.

probable hopping distance (R) and hopping energy (W) using following equations[31]:

$$R = \left[\frac{9L}{8\pi k_B T N(E)} \right]^{1/4}$$

and

$$W = \frac{3}{4\pi R^3 N(E)}$$

The hopping distance (R) at 300 K come out to be 4.12×10^{-7} cm and hopping energy (W) is 1.25 eV for $\text{Na}_{0.6}\text{MnO}_2$ sample. These values fulfill the requirements of Mott VRH conduction, which are $R/L > 1$ and $W > k_B T$, inferring that the conduction takes place via variable range hopping in $\text{Na}_{0.6}\text{MnO}_2$. However, for $\text{Na}_{0.7}\text{CoO}_2$ the hopping energy slightly higher (1 meV) than the $k_B T$ at 200 K, possibly due to the difference in estimated and actual localization length for $\text{Na}_{0.7}\text{CoO}_2$. We now discuss the observation of the strong electron localization in $\text{Na}_{0.6}\text{MnO}_2$, and there can be two plausible

reasons for such strong localization: first the presence of Mn^{3+} and Mn^{4+} where only Mn^{3+} is strong Jahn-Teller active, which makes the system strongly disorder and hence highly insulating [13]. As discussed above, the finding that the VRH conduction is taking place in this sample support this possibility. Also, a cooperative Jahn-Teller distortion coupled with Na vacancy ordering and charge ordering of Mn^{3+} and Mn^{4+} have recently been observed in $\text{Na}_{5/8}\text{MnO}_2$ [32]. This suggest the second possibility, which is the charge ordering of Mn^{3+} and Mn^{4+} . However, charge ordering generally takes place at lower temperatures in TM oxides and the temperature range of fitting is very high. Therefore, further investigation is required to pin point exact reason for the highly insulating behavior observed in $\text{Na}_{0.6}\text{MnO}_2$.

We now move to the discussion of magnetic behavior of these Na_xTO_2 ($T = \text{Mn, Co}$). The magnetic ground state in Na_xTO_2 is a result of super exchange interaction between neighboring T ions and whether the interaction is antiferromagnetic (AFM) or ferromagnetic (FM) de-

depends upon the valence states of these ions. The valence state not only determines the redox potential but also the structural stability of the electrode. For example in the case of $T=\text{Mn}$, the higher concentration of Mn^{3+} means higher Jahn teller distortion and thus a poor cycling performance [22]. Recent study shows that for an optimum insertion of Na/Li/K ion in MnO_2 layered structure give rise to a FM ground in an otherwise AFM lattice [33]. The study indicates that the storage of these alkali metals and magnetic ground states of host are correlated.

In order to get the insight of the magnetic ground state of $\text{Na}_{0.6}\text{MnO}_2$, which is largely unexplored for this composition [34], we first performed temperature dependent magnetization (M - T) as shown in Fig. 5 (a, c). The zero field cooled (ZFC) and field cooled (FC) curves do not show any transition till 5 K indicating the absence of long range magnetic ordering in both the samples. However, the inverse susceptibility (χ^{-1}) versus temperature plots [insets of Figs. 5 (a, c)] deviate from the Curie-Weiss behavior below 100-120 K. The susceptibility obeys the Curie-Weiss law at high temperatures from 100–120 K to 380 K. The Curie constant (C) and θ comes out as 2.71 and -403 K, respectively from the fitting for $\text{Na}_{0.6}\text{MnO}_2$ sample. Also, the effective magnetic moment (μ_{eff}) has been calculated from the Curie constant, which found to be $4.65 \mu_B$. By taking the proportion of Mn^{3+} (high spin) and Mn^{4+} in accordance with $\text{Na}_{0.6}\text{MnO}_2$, the theoretically calculated value of μ_{eff} is about $4.5 \mu_B$, which is very close to the experimentally observed value.

In order to confirm the absence of long range magnetic ordering we performed magnetic field dependent magnetization at 20 K as shown in Figs. 5(b, d). The magnetic isotherm plots show a typical paramagnetic behavior for both the samples with a very small hysteresis of 40–50 Oe. Similar magnetic behavior has been reported in Co substituted NaMnO_2 samples [35]. It is quite interesting that despite of a possible antiferromagnetic interaction between Mn^{3+} - Mn^{3+} and ferrimagnetic between Mn^{3+} and Mn^{4+} , this sample shows a paramagnetic behavior [32]. In the case of $\text{Na}_{0.7}\text{CoO}_2$, a small peak around 60 K is observed in the M - T data [Fig. 5(c)], which could be due to small contamination of oxygen at the sample surface as the SQUID is highly sensitive. For $\text{Na}_{0.7}\text{CoO}_2$, we found that Curie-Weiss constants C and θ are 0.52 and -719 K, which gives the effective magnetic moment of about $2.1 \mu_B$. As the Na concentration is lower than one, Co ions present in both 3+ and 4+ oxidation states and can exist in low spin (LS), intermediate state (IS), high spin (HS) or combination of mixed states. Therefore, by taking Co^{4+} in LS and Co^{3+} in mixed of LS and IS states (30% and 70%), we have calculated the theoretical magnetic moment, which turned out to be the calculated value of $\mu_{eff} = 2.1$. Our magnetization study confirm the variable oxidation states of TM ions, which are important for the performance of cathode materials.

Finally, we discuss electrochemical characterizations of

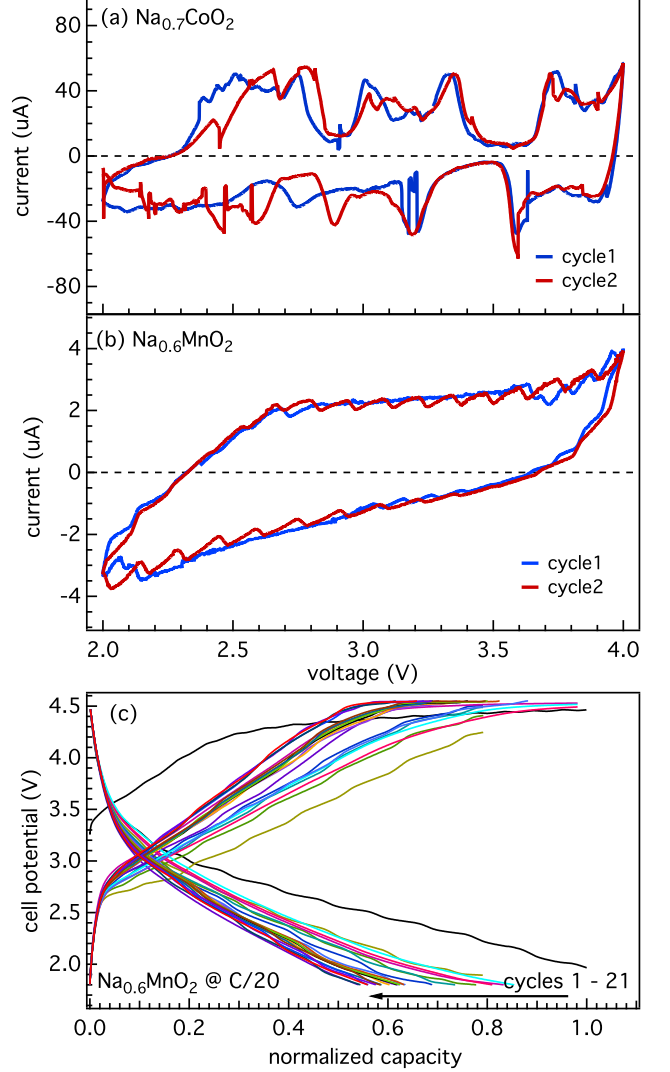


FIG. 6. The cyclic voltammetry (CV) characterization of fabricated coin cells of (a) $\text{Na}_{0.7}\text{CoO}_2$ and (b) $\text{Na}_{0.6}\text{MnO}_2$ with NaClO_4 as the electrolyte and metallic Na as the counter electrode, measured between 2.0–4.0 V at a scan rate of 0.1 mV/s. (c) The normalized capacity of $\text{Na}_{0.6}\text{MnO}_2$ coin-cell.

prepared coin cells using $\text{Na}_{0.7}\text{CoO}_2$ and $\text{Na}_{0.6}\text{MnO}_2$ as working electrode against Na counter electrode. Figs 6(a, b) show the cyclic voltammograms (CV) of both the electrodes for first few cycles, measured between 2.0–4.0 V at a scan rate of 0.1 mV/s at 20°C. In the CV curves of $\text{Na}_{0.7}\text{CoO}_2$, we observed several peaks during anodic as well as the corresponding cathodic scans which is in agreement with the literature [5, 36–38]. This confirms the reversibility of Na-ions and indicates the presence of various intermediate valence states during intercalation/de-intercalation of Na-ion in the solid matrix of the $\text{Na}_{0.7}\text{CoO}_2$. Similarly in the case of $\text{Na}_{0.6}\text{MnO}_2$ a multiphase evolution is observed during cycling as depicted by the presence of manifold ox-

idation and reduction peaks, which is common feature for Na_xMnO_2 [22, 39, 40]. The galvanostatic charging-discharging profile for $\text{Na}_{0.6}\text{MnO}_2$ is shown in Fig. 6(c), for first 21 cycles at current rate of 8 mA/g. We show the normalized capacity in Fig. 6(c) since the measured charge/discharge profiles of $\text{Na}_{0.6}\text{MnO}_2$ coin cells exhibit capacity that is lower than the theoretical value. The curves shows plateaus consistent with the multiphase evolution seen in CV. Each plateau correspond to extraction of Na ion from different sites. The capacity degradation upon cycling is fast and is in agreement with the earlier report [22] which is owing to the presence of Jahn-Teller Mn^{3+} ion. However, the durability for $T = \text{Co}$ is better [21] due to the absence of Jahn-Teller distortion.

CONCLUSIONS

In conclusion, we have synthesized a stable hexagonal phase of Na_xTO_2 ($T = \text{Mn}, \text{Co}$) and report the structure, morphology, magnetic ordering and electronic ground state, which play crucial role in determining the electrochemical properties of these compounds in Na-ion battery applications. The $\text{Na}_{0.6}\text{MnO}_2$ sample is highly insulating and the conduction takes place by variable range hopping of charge carriers even at higher temperatures. One the other hand $\text{Na}_{0.7}\text{CoO}_2$ shows semiconducting nature and conduct via activation and variable range hopping at high and low temperatures, respectively. Despite of the presence of magnetic Mn/Co^{3+} and Mn/Co^{4+} , a long range magnetic ordering is absent in these nanostructured samples till low temperatures. The cyclic voltammogram curves of the electrodes indicate the reversibility of Na-ions during intercalation/de-intercalation. The capacity degradation is fast in $\text{Na}_{0.6}\text{MnO}_2$ possibly due to structural distortion upon cycling and the presence of Jahn-Teller Mn^{3+} ion compare to $\text{Na}_{0.7}\text{CoO}_2$.

ACKNOWLEDGMENTS

We acknowledge the financial support from IIT Delhi through the FIRP project (no. MI01418). MC, and RS thank SERB-DST (NPDF, no PDF/2016/003565), and MHRD, respectively, for the fellowship. MC and MR also thank IIT Delhi for postdoctoral fellowship through FIRP project. Priyanka is thanked for useful discussions. Authors acknowledge IIT Delhi for providing research facilities: XRD, Raman, PPMS EVERCOOL-II at physics department, and EDX, SEM, TEM at CRF. We also thank the physics department, IIT Delhi for support. RSD thank SERB-DST for support through Early Career Research (ECR) Award (project reference no. ECR/2015/000159) and BRNS for support through DAE Young Scientist Research Award (project sanction no. 34/20/12/2015/BRNS).

* These authors contributed equally to this work

† rsdhaka@physics.iitd.ac.in

- [1] N. Yabuuchi, M. Kajiyama, J. Iwatate, H. Nishikawa, S. Hitomi, R. Okuyama, R. Usui, Y. Yamada, and S. Komaba, *Nature Materials* **11**, (2012) 512.
- [2] L. P. Wang, L. Yu, X. Wang, M. Srinivasan, and Z. J. Xu, *J. Mater. Chem. A* **3**, (2015) 9353.
- [3] H. Su, S. Jaffer, and H. Yu, *Energy Storage Materials* **5**, (2016) 116.
- [4] M. V. Reddy, G. V. Subba Rao, and B. V. R. Chowdari *Chem. Rev.* **113**, (2013) 5364.
- [5] R. Berthelot, D. Carlier, and C. Delmas, *Nature Materials* **10**, (2011) 74.
- [6] G.-L. Xu, R. Amine, Y.-F. Xu, J. Liu, J. Gim, T. Ma, Y. Ren, C.-J. Sun, Y. Liu, X. Zhang, S. M. Heald, A. Solhy, I. Saadoun, W. L. Mattis, S.-G. Sun, Z. Chen, and K. Amine, *Energy and Environmental Science* **10**, (2017) 1677.
- [7] M. V. Reddy, A. Sakunthala, S. SelvashekaraPandian, and B. V. R. Chowdari, *J. Phys. Chem. C* **117** (18), (2013) 9056.
- [8] K.S. Tan, M.V. Reddy, G.V. Subba Rao, B.V.R. Chowdari, *J. Power Sources* **147**, (2005) 241.
- [9] N. Nitta, F. Wu, J. T. Lee, and G. Yushin, *Materials Today* **18**, (2015) 252.
- [10] K. Mizushima, P. C. Jones, P. J. Wiseman, and J. B. Goodenough, *Materials Research Bulletin* **15**, (1980) 783.
- [11] M. H. Han, E. Gonzalo, G. Singha, and T. Rojo, *Energy and Environmental Science* **8**, (2015) 81.
- [12] C. Delmas, J. Braconnier, C. Fouassier, and P. Hagenmuller, *Solid State Ionics* **3**, (1981) 165.
- [13] A. Mendiboure, C. Delmas, and P. Hagenmuller, *J. Solid State Chem.* **57**, (1985) 323.
- [14] H. Kishan, V. P. S. Awana, M. A. Ansari, A. Gupta, R. B. Saxena, V. Ganesan, A. V. Narlikar, C. A. Cardoso, R. Nirmala, D. Buddhikot, and S. K. Malik, *J. of Appl. Phys.* **97**, (2005) 10A904.
- [15] N. Bucher, S. Hartung, A. Nagasubramanian, Y. L. Cheah, H. E. Hoster, and S. Madhavi, *ACS Appl. Mater. Interfaces* **6**, (2014) 8059.
- [16] Y. Cao, L. Xiao, W. Wang, D. Choi, Z. Nie, J. Yu, L. V. Saraf, Z. Yang, and J. Liu, *Adv. Mater.* **23**, (2011) 3155.
- [17] M. Xu, Y. Niu, C. Chen, J. Song, S. Bao, and C. M. Li, *RSC Adv.* **4**, (2014) 38140.
- [18] X. Ma, K. An, J. Bai, and H. Chen, *Nat. Sci. Rep.* **7**:162, (2017).
- [19] F. P. Nkosi, K. Raju, N. Palaniyandy, M. V. Reddy, C. Billing, and K. I. Ozoemena, *J. Electrochem. Soc.* **164**(13), (2017) A3362.
- [20] J.-P. Parant, R. Olazcuaga, M. Devalette, C. Fouassier, and P. Hagenmuller, *J. of Solid State Chem.* **3**, (1971) 1.
- [21] L. W. Shacklette, T. R. Jow, and L. Townsend, *J. Electrochem. Soc.* **135**, (1988) 2669.
- [22] A. Caballero, L. Hernán, J. Morales, L. Sánchez, J. S. Peña, and M. A. G. Aranda, *J. Mater. Chem.* **12**, (2002) 1142.
- [23] E. I. Suvorova, and P. A. Buffat, *Journal of Microscopy*, **196**, (1999), 46.
- [24] Y. Liu, Y. Qiao, X. Lou, X. Zhang, W. Zhang, and Y. Huang, *ACS Appl. Mater. Interfaces* **8**, (2016) 14564.

- [25] N. Karikalan, C. Karuppiyah, S.-M. Chen, M. Velmurugan, and P. Gnanaprakasam, *Chem. Eur. J.* **23**, (2017) 2379.
- [26] L. Zhao, J. Ni, H. Wang, and L. Gao, *RSC Advances* **3**, (2013) 6650.
- [27] M.N. Iliev, A.P. Litvinchuk, R.L. Meng, Y.Y. Sun, J. Cmaidalka, and C.W. Chu, *Physica C* **402**, (2004) 239.
- [28] Y. G. Shi, Y. L. Liu, H. X. Yang, C. J. Nie, R. Jin, and J. Q. Li, *Phys. Rev. B* **70**, (2004) 052502.
- [29] P. Lemmens, K. Y. Choi, V. Gnezdilov, E. Ya. Sherman, D. P. Chen, C. T. Lin, F. C. Chou, and B. Keimer **96**, (2006) 167204.
- [30] N. F. Mott, 2nd ed. (Taylor and Francis, London, 1990).
- [31] M. Viret, L. Ranno, and J. M. D. Coey, *Phys. Rev. B.* **55**, (1997) 8067.
- [32] X.Li, X. Ma, D. Su, L. Liu, R. Chisnell, S. P. Ong, H. Chen, A. Toumar, J.-C. Idrobo, Y. Lei, J. Bai, F. Wang, J. W. Lynn, Y. S. Lee, and G. Ceder, *Nature Materials* **13**, (2014) 586.
- [33] Li-T. Tseng, Y. Lu, H. M.Fan, Y. Wang, X. Luo,T. Liu, P. Munroe, S. Li, and Jiabao Yi, *Nat. Sci. Rep.* **5**, (2016) 9094.
- [34] A. M. Abakumov, A.A. Tsirlin, I. Bakaimi, G. V. Tendeloo, and A. Lappas, *Chem. Mater.* **26**, (2014) 3306.
- [35] D. Carlier, J. H. Cheng, R. Berthelot, M. Guignard, M. Yoncheva, R. Stoyanova, B. J. Hwang, and C. Delmas, *Dalton Trans.* **40**, (2011) 9306.
- [36] B. V. R. Reddy, R. Ravikumar, C. Nithyab, and S. Gopukumar, *J. Mater. Chem. A* **3**, (2015)18059.
- [37] A. Bhide, J. Hofmann, A. K. Dürr, J. Janeka, and P. Adelhelm, *Phys. Chem. Chem. Phys.* **16**, (2014) 1987.
- [38] F. Sauvage, L. Laffont, J.-M Tarascon, and E. Baudrin, *Inorg. Chem.* **46**, (2007) 3289.
- [39] X. Ma, H. Chen, and G. Ceder, *J. of The Electrochemical Society* **158**, (2011) A1307.
- [40] N. Bucher, S. Hartung, I. Gocheva, Y. L. Cheah, M. Srinivasan, and H. E. Hoster, *J. Solid State Electrochem.* **17**, (2013) 1923.